Current Oncology

MDPI

Article

Contrast-Enhanced CT-Based Stratification of CLDN18.2 Expression Levels in Gastric Cancer: A Retrospective Model-Development Study

Fangjing Hou [1,†], Yiting Liu [1,†], Jieyuan Cai [2,3], Wanying Ji [1], Jiazheng Li [1], Xiaoting Li [1], Xiaotian Zhang [2], Yu Sun [4,*] and Lei Tang [1,*]

[1] Key Laboratory of Carcinogenesis and Translational Research (Ministry of Education), Department of Radiology, Peking University Cancer Hospital and Institute, Beijing 100142, China; 2311110703@bjmu.edu.cn (F.H.)
[2] Key Laboratory of Carcinogenesis and Translational Research (Ministry of Education/Beijing), Department of Gastrointestinal Oncology, Peking University Cancer Hospital and Institute, 52 Fucheng Road, Hai-Dian District, Beijing 100142, China; zhangxiaotian@bjmu.edu.cn (X.Z.)
[3] Department of Radiation Oncology, Clinical Oncology School of Fujian Medical University, Fujian Cancer Hospital, Fuzhou 350014, China
[4] State Key Laboratory of Holistic Integrative Management of Gastrointestinal Cancers, Department of Pathology, Peking University Cancer Hospital and Institute, Beijing 100142, China
* Correspondence: sunyu_bch@163.com (Y.S.); tanglei@pku.edu.cn (L.T.)
† These authors contributed equally to this work.

Simple Summary

Claudin 18 isoform 2 (CLDN18.2) is a therapeutic target in gastric cancer and is assessed using tissue immunohistochemistry. However, biopsy samples may not fully represent spatially heterogeneous tumours. We investigated whether routine contrast-enhanced computed tomography (CT) could provide complementary whole-lesion information on CLDN18.2 expression in 222 patients with untreated gastric adenocarcinoma. Readily interpretable CT features were associated with CLDN18.2 positivity, and their integration with clinicopathological information provided modest incremental discrimination. Model-derived probabilities increased across ordered expression categories, but the models did not reliably identify the 40–74% intermediate-expression group or accurately estimate individual staining percentages. Rather than determining who should undergo initial CLDN18.2 testing, CT may provide an additional clue when imaging and immunohistochemical findings are discordant, prompting review of specimen adequacy, staining quality, and spatial heterogeneity. Immunohistochemistry remains the reference standard for determining CLDN18.2 status. Multicentre external validation is required before this complementary role can be implemented clinically.

Abstract

Background: Claudin 18 isoform 2 (CLDN18.2) is a therapeutic target in gastric cancer. We evaluated whether routine contrast-enhanced computed tomography (CT) features were associated with CLDN18.2 expression and could complement tissue assessment. Methods: This retrospective study included 222 patients with untreated gastric adenocarcinoma. CLDN18.2 positivity was defined as moderate-to-strong membranous staining in at least 40% of tumour cells. Clinicopathological, CT feature, and Integrated logistic regression models were developed and internally validated using 1000 bootstrap resamples. Integrated-model probabilities were examined across ordered expression strata, and the same uniformly shrunken model score was applied to the ≥75% outcome without outcome-specific refitting. Ordinal and continuous expression models were assessed using repeated cross-validation.

Check for updates

Received: 10 October 2026
Revised: 22 November 2026
Accepted: 26 November 2026
Published: 29 November 2026

Copyright: © 2026 by the authors. Licensee MDPI, Basel, Switzerland. This article is an open access article distributed under the terms and conditions of the Creative Commons Attribution (CC BY) license.

Results: CLDN18.2 positivity occurred in 130 patients (58.6%). The Integrated model achieved an apparent area under the receiver operating characteristic curve (AUC) of 0.773 (95% CI, 0.707–0.834) and an optimism-corrected AUC of 0.735. The optimism-corrected AUCs were 0.706 for the clinicopathological model and 0.698 for the CT feature model. After uniform shrinkage, Integrated-model probabilities increased across the <40%, 40–74%, and ≥75% expression strata. Probabilities were higher in the ≥75% group than in the 40–74% group, with a moderate between-group effect (Cliff's delta for 40–74% versus ≥75%, −0.386; 95% confidence interval, −0.589 to −0.163). The cross-validated ordinal model yielded an ordinal C-index of 0.718 but poorly discriminated the 40–74% intermediate-expression group (class-specific AUC, 0.535). The continuous model yielded a cross-validated (R^2) of 0.217. When applied without refitting to the ≥75% outcome, the same shrunken Integrated-model score yielded an AUC of 0.781; this within-cohort discrimination was partly expected because all ≥75% cases had been included in the positive class used for model development. Conclusions: Routine contrast-enhanced CT features provide an interpretable whole-lesion phenotype associated with CLDN18.2 expression. The phenotype reflects an ordered group-level association with expression but does not reliably identify the intermediate-expression group or estimate individual staining percentages. CT may complement immunohistochemistry when imaging and tissue findings are discordant, while immunohistochemistry remains the reference standard for determining CLDN18.2 status.

Keywords: gastric cancer; CLDN18.2; contrast-enhanced computed tomography; immunohistochemistry; computed tomography; imaging biomarker; risk stratification

1. Introduction

Gastric cancer diagnosis and initial staging generally combine endoscopic biopsy for histological and molecular assessment with contrast-enhanced CT for locoregional and distant staging [1]. Together, these assessments inform multidisciplinary, biomarker-guided treatment planning [1,2]. Claudin 18 isoform 2 (CLDN18.2) has emerged as a clinically applicable therapeutic target for advanced gastric cancer. In the phase 3 SPOTLIGHT and GLOW trials, first-line zolbetuximab plus chemotherapy significantly improved progression-free and overall survival in patients with CLDN18.2-positive, HER2-negative, locally advanced unresectable, or metastatic gastric adenocarcinoma [3,4]. These findings establish CLDN18.2-directed therapy as an important treatment option and promote the incorporation of CLDN18.2 testing into biomarker-guided treatment selection. Therefore, accurate assessment of tumour CLDN18.2 expression is essential to identifying patients who may benefit from zolbetuximab-based therapy.

CLDN18.2, a gastric lineage-specific tight-junction protein, is exposed on the tumour cell surface after loss of epithelial polarity during malignant transformation [5]. This altered membrane localisation provides a rationale for antibody-based therapeutic targeting [6]. CLDN18.2 positivity has been assessed using moderate-to-strong membranous staining in at least 40% of tumour cells in exploratory studies, whereas the phase 3 SPOTLIGHT and GLOW trials used a threshold of at least 75% [3,4,7]. However, tissue immunohistochemistry (IHC)-based assessment of CLDN18.2 remains dependent on local sampling and may not fully reflect whole-tumour expression. Intratumoural heterogeneity limits the sensitivity of small biopsy specimens. A single virtual biopsy identified CLDN18.2 positivity with a sensitivity of 58.8% compared to whole-section assessment, increasing to 76.5% with six–eight tumour-bearing biopsies [8]. Discordance between primary and metastatic lesions has been reported in approximately 18% to 25% of patients [8,9]. A small paired-sample study reported loss of CLDN18.2 positivity at disease progression after zolbetuximab-

containing therapy [10]. Differences in antibody platforms and positivity thresholds further contribute to the variability in reported prevalence estimates [11,12].

Contrast-enhanced CT is routinely performed for gastric cancer staging and provides readily available information on the tumour location, morphology, enhancement characteristics, nodal involvement, and metastatic spread. Previous studies have demonstrated an association between CT findings and the molecular phenotypes in gastric cancer. HER2-positive gastric cancers have been associated with characteristic findings on conventional CT [13,14], while CT-based radiomics and deep-learning approaches have also been investigated for predicting HER2 status [15,16]. CT features including mucosal line interruption, diffuse wall thickening, and infiltrative margins have also been reported to differentiate poorly cohesive carcinoma [17]. Previous CLDN18.2 imaging studies have investigated targeted PET tracers and conventional [^{18}F]FDG PET/CT [18–22], while recent CT radiomics studies have also reported associations with CLDN18.2 expression [23,24]. However, evidence linking directly assessable and measurable features on routine contrast-enhanced CT with CLDN18.2 expression remains limited. Whether these conventional CT features are associated with ordered CLDN18.2 expression levels also warrants investigation. IHC provides a localised assessment of sampled tissue, while contrast-enhanced CT may provide complementary whole-lesion information through macroscopic phenotypes associated with CLDN18.2 expression. CT-derived probabilities may provide additional context for interpreting IHC results and considering tissue sampling adequacy. Future studies integrating spatial radiology–pathology correlations may further investigate whether CT features can characterise CLDN18.2-enriched regions within tumours and inform biopsy site selection.

This study aimed to evaluate the association between routine contrast-enhanced CT features and CLDN18.2 expression and to develop and internally validate clinicopathological, CT feature, and Integrated models using the ≥40% definition. We further examined whether the Integrated-model score was associated with ordered CLDN18.2 expression levels and assessed its discrimination for the ≥75% outcome within the same cohort. Ordinal and continuous expression models were evaluated as sensitivity analyses.

2. Materials and Methods

2.1. Patients

This retrospective study was conducted in accordance with the Declaration of Helsinki and was approved by the Ethics Committee of Peking University Cancer Hospital (approval No. 2023KT59), and the requirement for informed consent was waived. Patients with pathologically confirmed gastric adenocarcinoma were identified between June 2019 and April 2021. Eligibility criteria included pathologically confirmed gastric adenocarcinoma, available CLDN18.2 IHC results, absence of prior antitumor therapy before baseline imaging, complete contrast-enhanced abdominopelvic CT examinations, and complete clinical documentation. Patients were excluded if they had received any antitumor therapy before the baseline CT examination, had synchronous or previous primary malignancies, had no measurable lesion on baseline CT, or had significant motion artefacts or inadequate gastric distension on contrast-enhanced images. The final cohort included 222 patients (Figure 1).

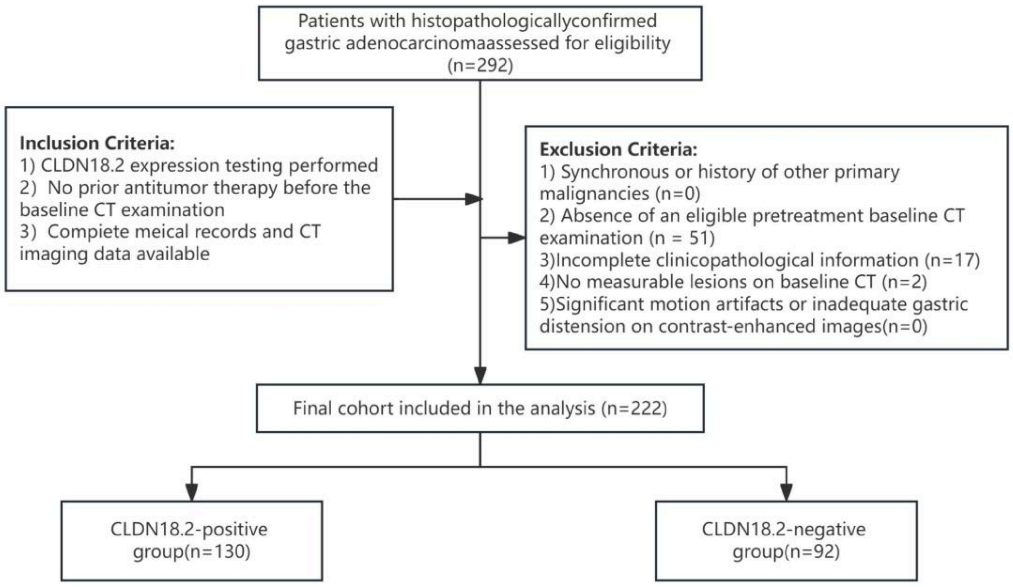


Figure 1. Study flow.

2.2. CLDN18.2 Immunohistochemistry

CLDN18.2 expression was evaluated using formalin-fixed, paraffin-embedded tissue specimens. After deparaffinisation, rehydration, and heat-induced epitope retrieval, non-specific binding was blocked using ZSBIO ZLI-9056 solution. The sections were incubated with a rabbit monoclonal anti-CLDN18.2 antibody (clone EPR19202; ab222512; Abcam Ltd., Cambridge, UK; 1:300 dilution) and detected using a universal SAP secondary antibody system (SAP-9100; Beijing Zhongshan Golden Bridge Biotechnology Co., Ltd., Beijing, China). Two pathologists with 4 and 20 years of experience in pathological diagnosis independently evaluated membranous staining, and discrepancies were resolved by consensus. The primary model development definition required moderate-to-strong membranous staining in at least 40% of tumour cells, consistent with a previously reported cutoff [7]. Cross-definition analysis used the clinically relevant cutoff of moderate-to-strong membranous staining in at least 75% of tumour cells, as applied in the phase 3 SPOTLIGHT and GLOW trials [3,4]. The IHC results served as the reference standard.

2.3. CT Acquisition

The patients fasted for at least 6 h before the CT examination. Unless contraindicated, 10 mg of raceanisodamine hydrochloride (654-2; Hangzhou Minsheng Pharmaceutical Co., Ltd., Hangzhou, China) was administered intramuscularly to reduce gastrointestinal peristalsis, followed by 6 g of effervescent granules (Qingdao Hongdie New Materials Co., Ltd., Qingdao, China) and 10 mL of water for gastric distension. CT examinations were performed from the diaphragmatic dome to the inferior pubic symphysis using GE Optima CT680 and GE Discovery CT750 HD scanners (GE Healthcare, Milwaukee, WI, USA). Nonionic iodinated contrast material (Omnipaque 300, 300 mg I/mL; GE Healthcare) was administered intravenously at a rate of 3.5 mL/s (1.5 mL/kg). Arterial- and venous-phase images were acquired 35–40 s and 70 s after contrast injection, respectively. Multiplanar reconstruction was performed using a slice thickness of 5 mm.

2.4. Image Analysis

Two abdominal radiologists with 10 and 6 years of experience in oncologic imaging independently reviewed the CT examinations while being blinded to the CLDN18.2 expression status and pathological findings. The basic tumour characteristics included location,

Borrmann type, esophagogastric junction involvement, and circumferential extent. The maximum tumour length and thickness were measured. The transition morphology was classified as either elevated or sloped. An elevated transition was defined as at least two abrupt angles, whereas a sloped transition showed a smooth interface with the adjacent gastric wall. Enhancement pattern, degree of enhancement, and peak enhancement phase were recorded. Peritoneal metastasis, ascites, and distant metastasis were evaluated based on CT findings.

Nodal assessment included CT-based N stage and measurement of the short-axis diameter of the largest lymph node. Bulky lymph nodes were defined as those with a short-axis diameter ≥ 3 cm. Additional nodal characteristics included heterogeneous enhancement, nodal confluence, clustered peritumoural nodes, and morphologically abnormal retroperitoneal nodes. Clustered nodes were defined as the aggregation of at least five lymph nodes surrounding the primary tumour.

Tumour attenuation was measured on unenhanced, arterial-phase, and venous-phase images using circular regions of interest (ROIs). The venous-phase image was used as the reference. The ROI was placed at the site of greatest tumour thickness on the axial image showing the maximal tumour extent. Matched ROIs were then placed at the corresponding tumour location on the unenhanced and arterial-phase images, with the ROI size maintained as closely as possible. Minor positional adjustments were allowed to account for respiratory motion or displacement of the gastric wall between phases. Aortic attenuation was measured during the corresponding phases, and normalised tumour enhancement ratios were calculated as tumour attenuation divided by aortic attenuation. Representative CT images and measurement schematics are provided in Supplementary Table S1.

2.5. Statistical Analysis

No clinically relevant data were missing. Continuous variables were presented as means ± standard deviations or medians with interquartile ranges, as appropriate, and categorical variables were presented as counts and percentages. Continuous variables were compared using the Wilcoxon rank-sum test, and categorical variables were compared using the chi-square test or Fisher's exact test, as appropriate. Univariable logistic regression was used to estimate odds ratios (ORs) and 95% confidence intervals (CIs) for associations with CLDN18.2 positivity under the primary ≥40% definition.

Candidate predictors sets were data-informed and defined before multivariable model fitting. Predictor selection considered clinical relevance, measurement reliability, redundancy between variables, the number of outcome events, model complexity, and univariable associations with CLDN18.2 positivity at $p < 0.05$. Multicollinearity was assessed using variance inflation factors (VIFs). All selected predictors were entered simultaneously into the corresponding multivariable logistic regression models; no automated variable-selection procedure was used in the primary analysis. Clinical variables were incorporated into the clinical model, CT features into the CT feature model, and both domains into the integrated model. Model performance was assessed using the area under the receiver operating characteristic curve (AUC), the Brier score, calibration plots, calibration intercept and slope.

Internal validation used 1000 nonparametric bootstrap resamples. In each resample, all coefficients were re-estimated using the fixed data-informed predictor set, and model performance was evaluated in both the bootstrap sample and the original dataset. Optimism-corrected AUC, Brier score, calibration intercept, and calibration slope were obtained by subtracting the mean bootstrap optimism from the apparent estimates. Bootstrap distributions of the regression coefficients were also examined to assess coefficient stability. For the Integrated model, the optimism-corrected calibration slope of 0.815 was used as a uniform

shrinkage factor. All nine slope coefficients were multiplied by 0.815, and the intercept was re-estimated to preserve calibration-in-the-large.

The resulting Integrated-model probabilities were evaluated across the <40%, 40–74%, and ≥75% expression strata. Overall and pairwise group differences, the effect size for the comparison between the two higher-expression groups, ordinal associations, and trends across model-score quintiles were assessed. The same model score was evaluated against the ≥75% outcome without outcome-specific refitting. Detailed predictor selection, model comparisons, validation procedures, HER2 subgroup analyses, and ordinal and continuous expression analyses are described in the Supplementary Methods. Reporting followed the Transparent Reporting of a multivariable prediction model for Individual Prognosis Or Diagnosis (TRIPOD) statement [25], and the completed checklist is provided as File S1.

All analyses were performed using IBM SPSS Statistics for Windows, version 26.0.0.1 (IBM Corp., Armonk, NY, USA), and R version 4.3.2 (R Foundation for Statistical Computing, Vienna, Austria) within RStudio, version 2026.01.0 Build 392 (Posit Software, PBC, Boston, MA, USA). Statistical significance was set at two-sided p-values < 0.05.

3. Results

3.1. Study Population and Clinicopathologic Characteristics

Among 222 patients, 130 (58.6%) were classified as CLDN18.2-positive and 92 (41.4%) as CLDN18.2-negative, using the 40% threshold (Figure 1). CLDN18.2-positive patients were more frequently aged ≤60 years (73.8% vs. 46.7%, $p < 0.001$) and female (40.8% vs. 25.0%, $p = 0.022$). Compared with CLDN18.2-negative tumours, CLDN18.2-positive tumours more frequently demonstrated diffuse or mixed Lauren histology (48.5% and 26.2% vs. 28.3% and 18.5%, respectively; $p < 0.001$), signet-ring cell carcinoma (48.5% vs. 22.8%, $p < 0.001$), and HER2-negative status (91.5% vs. 80.4%, $p = 0.027$) (Table 1).

Table 1. Clinical and pathological characteristics according to CLDN18.2 status.

Variable	Overall (N = 222)	CLDN18.2 Negative (n = 92)	CLDN18.2 Positive (n = 130)	*p*-Value
Age, years				<0.001
≤60	139 (62.6%)	43 (46.7%)	96 (73.8%)	
>60	83 (37.4%)	49 (53.3%)	34 (26.2%)	
Sex				0.022
Female	76 (34.2%)	23 (25.0%)	53 (40.8%)	
Male	146 (65.8%)	69 (75.0%)	77 (59.2%)	
Lauren classification				<0.001
Intestinal type	82 (36.9%)	49 (53.3%)	33 (25.4%)	
Diffuse type	89 (40.1%)	26 (28.3%)	63 (48.5%)	
Mixed type	51 (23.0%)	17 (18.5%)	34 (26.2%)	
Differentiation grade				0.042
Poorly differentiated	173 (77.9%)	65 (70.7%)	108 (83.1%)	
Moderately differentiated	46 (20.7%)	26 (28.3%)	20 (15.4%)	
Well differentiated	3 (1.4%)	1 (1.1%)	2 (1.5%)	
Signet-ring cell carcinoma				<0.001
Non-signet-ring cell carcinoma	138 (62.2%)	71 (77.2%)	67 (51.5%)	
Signet-ring cell carcinoma	84 (37.8%)	21 (22.8%)	63 (48.5%)	
HER2 expression				0.027
Negative	193 (86.9%)	74 (80.4%)	119 (91.5%)	
Positive	29 (13.1%)	18 (19.6%)	11 (8.5%)	

Data are presented as n (%). Group comparisons were performed using the chi-squared test or Fisher's exact test, as appropriate. CLDN18.2 positivity was defined as moderate-to-strong membranous staining in at least 40% of the tumour cells.

3.2. CT Features Associated with CLDN18.2 Expression

Routine CT features demonstrated an imaging phenotype associated with CLDN18.2 expression. CLDN18.2-positive tumours showed a lower frequency of esophagogastric junction involvement (24.6% vs. 44.6%, $p = 0.002$) and a higher frequency of Borrmann type IV morphology (26.9% vs. 8.7%, $p = 0.004$). In univariable analysis, lower-third tumours had higher odds of CLDN18.2 positivity than upper-third tumours (OR, 2.06; 95% CI, 1.02–4.18; $p = 0.045$), while the overall distribution across tumour locations yielded $p = 0.119$. CLDN18.2-positive tumours also demonstrated higher arterial-phase attenuation (75.2 ± 23.7 HU vs. 68.0 ± 23.5 HU, $p = 0.030$), a greater frequency of moderate or marked enhancement, and higher frequencies of peritoneal metastasis, ascites, and distant metastasis. Clustered lymph nodes were less frequent among the CLDN18.2-positive tumours (Table 2).

Table 2. Univariate analysis of CT features by CLDN18.2 expression status.

Variable	Overall (N = 222)	Negative (n = 92)	Positive (n = 130)	OR (95% CI)	*p*-Value
Tumour location					
Upper	83 (37.4%)	41 (44.6%)	42 (32.3%)	Reference	
Middle	83 (37.4%)	33 (35.9%)	50 (38.5%)	1.48 (0.80–2.74)	0.212
Lower	56 (25.2%)	18 (19.6%)	38 (29.2%)	2.06 (1.02–4.18)	0.045
EGJ involvement					
No	149 (67.1%)	51 (55.4%)	98 (75.4%)	Reference	
Yes	73 (32.9%)	41 (44.6%)	32 (24.6%)	0.41 (0.23–0.72)	0.002
Borrmann type					
Type II	15 (6.8%)	9 (9.8%)	6 (4.6%)	Reference	
Type III	164 (73.9%)	75 (81.5%)	89 (68.5%)	1.78 (0.61–5.23)	0.294
Type IV	43 (19.4%)	8 (8.7%)	35 (26.9%)	6.56 (1.81–23.77)	0.004
T stage					
T2	5 (2.3%)	3 (3.3%)	2 (1.5%)	Reference	
T3	54 (24.3%)	24 (26.1%)	30 (23.1%)	1.88 (0.29–12.14)	0.510
T4	163 (73.4%)	65 (70.7%)	98 (75.4%)	2.26 (0.37–13.91)	0.379
N stage					
N0	53 (23.9%)	19 (20.7%)	34 (26.2%)	Reference	
N1	41 (18.5%)	15 (16.3%)	26 (20.0%)	0.97 (0.42–2.26)	0.941
N2	74 (33.3%)	34 (37.0%)	40 (30.8%)	0.66 (0.32–1.36)	0.256
N3	54 (24.3%)	24 (26.1%)	30 (23.1%)	0.70 (0.32–1.52)	0.365
Tumour length (mm)	92.3 ± 46.5	86.8 ± 45.0	96.1 ± 47.4	1.05 (0.99–1.11)	0.141
Tumour thickness (mm)	17.1 ± 6.2	16.8 ± 6.7	17.3 ± 5.8	1.01 (0.97–1.06)	0.568
Rolled edge					
No	203 (91.4%)	81 (88.0%)	122 (93.8%)	Reference	
Yes	19 (8.6%)	11 (12.0%)	8 (6.2%)	0.48 (0.19–1.27)	0.260
Morphology					
Slope	147 (66.2%)	57 (62.0%)	90 (69.2%)	Reference	
Elevated	75 (33.8%)	35 (38.0%)	40 (30.8%)	0.72 (0.41–1.25)	0.134

Table 2. *Cont.*

Variable	Overall (N = 222)	Negative (n = 92)	Positive (n = 130)	OR (95% CI)	*p*-Value
Enhancement pattern					
Homogeneous	68 (30.6%)	26 (28.3%)	42 (32.3%)	Reference	
Heterogeneous non-layered	93 (41.9%)	46 (50.0%)	47 (36.2%)	0.63 (0.34–1.20)	0.158
Heterogeneous layered	61 (27.5%)	20 (21.7%)	41 (31.5%)	1.27 (0.62–2.62)	0.519
Enhancement degree					
Mild	61 (27.5%)	35 (38.0%)	26 (20.0%)	Reference	
Moderate	62 (27.9%)	23 (25.0%)	39 (30.0%)	2.28 (1.11–4.70)	0.025
Marked	99 (44.6%)	34 (37.0%)	65 (50.0%)	2.57 (1.34–4.96)	0.005
Enhancement peak					
Arterial	49 (22.1%)	26 (28.3%)	23 (17.7%)	Reference	
Venous	173 (77.9%)	66 (71.7%)	107 (82.3%)	1.83 (0.97–3.47)	0.063
Arterial-phase CT value (HU)	72.2 ± 23.8	68.0 ± 23.5	75.2 ± 23.7	1.01 (1.00–1.02)	0.030
Venous-phase CT value (HU)	79.2 ± 26.2	75.6 ± 28.1	81.7 ± 24.6	1.01 (1.00–1.02)	0.093
NTER (arterial phase)	0.35 ± 0.14	0.32 ± 0.13	0.37 ± 0.14	1.30 (1.06–1.60)	0.012
NTER (venous phase)	0.56 ± 0.17	0.53 ± 0.18	0.57 ± 0.15	1.18 (1.00–1.39)	0.053
Venous–arterial attenuation difference (HU)	7.0 ± 17.3	7.6 ± 21.1	6.5 ± 14.2	1.00 (0.98–1.01)	0.643
Clustered lymph nodes					
No	172 (77.5%)	64 (69.6%)	108 (83.1%)	Reference	
Yes	50 (22.5%)	28 (30.4%)	22 (16.9%)	0.47 (0.25–0.88)	0.019
Fused lymph nodes					
No	166 (74.8%)	63 (68.5%)	103 (79.2%)	Reference	
Yes	56 (25.2%)	29 (31.5%)	27 (20.8%)	0.57 (0.31–1.05)	0.071
Peritoneal metastasis					
No	141 (63.5%)	69 (75.0%)	72 (55.4%)	Reference	
Yes	81 (36.5%)	23 (25.0%)	58 (44.6%)	2.42 (1.35–4.34)	0.003
Ascites					
No	114 (51.4%)	60 (65.2%)	54 (41.5%)	Reference	
Yes	108 (48.6%)	32 (34.8%)	76 (58.5%)	2.64 (1.52–4.59)	<0.001
Distant metastasis					
No	102 (45.9%)	53 (57.6%)	49 (37.7%)	Reference	
Yes	120 (54.1%)	39 (42.4%)	81 (62.3%)	2.25 (1.30–3.87)	0.004

Categorical data are n (%); continuous data are means ± standard deviations (SDs). Odds ratios (ORs) and *p*-values were obtained using univariate logistic regression. ORs for tumour length are reported per 10-mm increase, and ORs for NTER are reported per 0.1-unit increase. The reference categories are listed in the table. NTER is the dimensionless tumour-to-aorta attenuation ratio. The venous–arterial difference equals the venous-phase minus the arterial-phase tumour attenuation. CI, confidence interval; EGJ, esophagogastric junction; HU, Hounsfield unit; LN, lymph node; NTER, normalised tumour enhancement ratio.

3.3. Interobserver Agreement

Interobserver agreement was good to excellent for the continuous CT measurements included in the agreement analysis, with ICCs ranging from 0.891 to 1.000. The venous-minus-arterial tumour attenuation difference showed the lowest agreement (ICC, 0.891; 95% CI, 0.860–0.916). The Bland–Altman analysis demonstrated small mean biases relative to the measurement scales, with feature-specific limits of agreement (Supplementary Table S2). Among the 20 categorical CT features, 19 showed almost perfect agreement with kappa values ranging from 0.916 to 1.000. Peak enhancement phase showed substantial agreement ($\kappa = 0.788$; 95% CI, 0.692–0.884), with discordant assessments in 17 of 222 patients (7.7%) (Supplementary Table S3).

3.4. Development of the Prediction Models Using the ≥40% Definition

The clinicopathological model included age, sex, HER2 status, and signet-ring cell carcinoma. The CT feature model included esophagogastric junction involvement, Borrmann type IV morphology, arterial-phase tumour attenuation, the presence of distant metastasis, and clustered peritumoural lymph nodes. The Integrated model contained all nine predictors. All predictors were entered simultaneously and retained. In the Integrated model, age > 60 years (OR, 0.40; 95% CI, 0.21–0.76; $p = 0.005$), HER2 positivity (OR, 0.38; 95% CI, 0.15–0.95; $p = 0.040$), and esophagogastric junction involvement (OR, 0.48; 95% CI, 0.24–0.95; $p = 0.035$) were associated with lower odds of CLDN18.2 positivity. Signet-ring cell carcinoma (OR, 2.45; 95% CI, 1.25–4.82; $p = 0.009$), Borrmann type IV morphology (OR, 2.98; 95% CI, 1.22–7.31; $p = 0.017$), and distant metastasis (OR, 1.99; 95% CI, 1.06–3.71; $p = 0.032$) were associated with higher odds. Arterial-phase tumour attenuation showed a positive association of borderline statistical significance (OR per HU, 1.014; 95% CI, 1.000–1.029; $p = 0.051$). Sex and clustered peritumoural lymph nodes were retained despite non-significant individual associations (Table 3 and Figure 2).

Table 3. Multivariable logistic regression analysis using the ≥40% definition.

Variable	Clinicopathological OR (95% CI)	*p*	CT Features OR (95% CI)	*p*	Integrated OR (95% CI)	*p*
Age > 60 years	0.36 (0.19–0.65)	<0.001	—	—	0.40 (0.21–0.76)	0.005
Male sex	0.69 (0.36–1.29)	0.245	—	—	1.31 (0.63–2.74)	0.469
HER2 positive	0.41 (0.17–0.95)	0.039	—	—	0.38 (0.15–0.95)	0.040
Signet-ring cell carcinoma	2.51 (1.34–4.68)	0.004	—	—	2.45 (1.25–4.82)	0.009
EGJ involvement	—	—	0.43 (0.23–0.81)	0.008	0.48 (0.24–0.95)	0.035
Borrmann IV vs. II/III	—	—	3.19 (1.36–7.49)	0.008	2.98 (1.22–7.31)	0.017
Arterial attenuation, per HU	—	—	1.012 (0.999–1.025)	0.071	1.014 (1.000–1.029)	0.051
Metastasis present	—	—	1.89 (1.05–3.40)	0.033	1.99 (1.06–3.71)	0.032
Clustered peritumoral LNs	—	—	0.49 (0.25–0.97)	0.041	0.73 (0.35–1.53)	0.403

The data-informed predictor sets were derived by considering univariable associations ($p < 0.05$), clinical relevance, measurement reliability, redundancy, the number of outcome events, and model complexity. All selected predictors were entered simultaneously and retained irrespective of their multivariable *p*-values. The Integrated model contained nine slope parameters. CI, confidence interval; EGJ, esophagogastric junction; HER2, human epidermal growth factor receptor 2; HU, Hounsfield unit; LN, lymph node; OR, odds ratio.

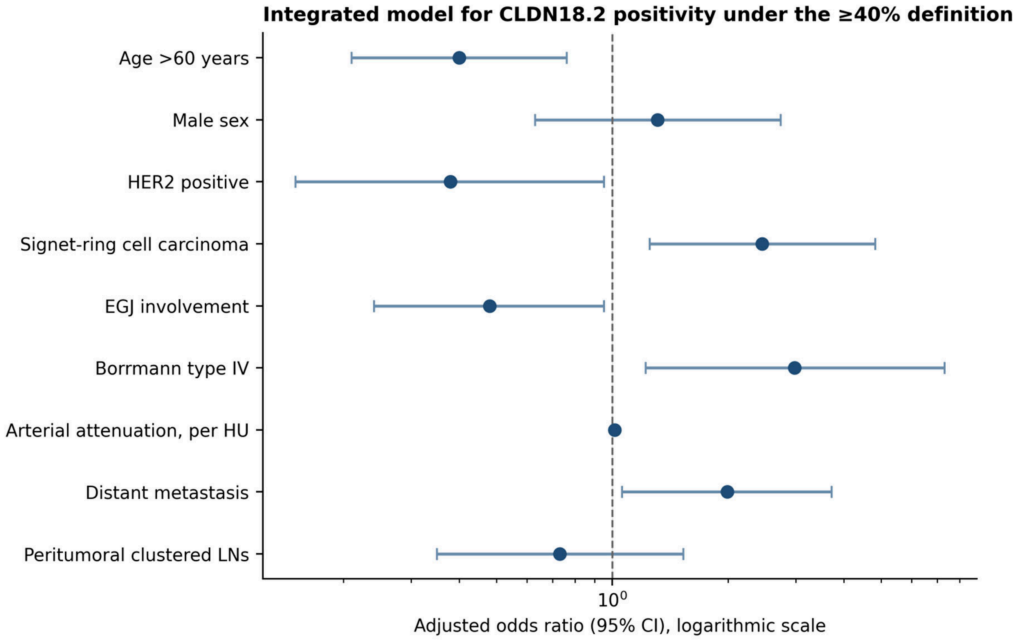


Figure 2. Forest plot of the Integrated model using the ≥40% definition. Adjusted odds ratios and 95% confidence intervals are shown for all nine predictors in the final candidate predictor set. All variables were entered simultaneously and retained irrespective of their multivariable *p*-values. The vertical dashed line indicates an odds ratio of 1. CI, confidence interval; EGJ, esophagogastric junction; HU, Hounsfield unit; LN, lymph node.

3.5. Model Performance and Internal Validation

The integrated model demonstrated the highest apparent discrimination (AUC, 0.773;95% CI, 0.707–0.834), followed by the clinical model (AUC, 0.724; 95% CI, 0.660–0.792) and the CT feature model (AUC, 0.722;95% CI, 0.653–0.785). The apparent AUC difference was 0.051 between the Integrated and CT feature models (95% bootstrap CI, 0.006–0.100). The corresponding apparent Brier scores were 0.189, 0.208, and 0.209, respectively (Table 4 and Figure 3).

Table 4. Apparent performance of the models.

Model	Apparent AUC	95% CI	Brier Score
Clinicopathological	0.724	0.660–0.792	0.208
CT features	0.722	0.653–0.785	0.209
Integrated	0.773	0.707–0.834	0.189

Values shown are apparent performance estimates from the development cohort and have not been corrected for optimism. Optimism-corrected AUC, Brier score, calibration intercept, and calibration slope are reported in Supplementary Table S4. AUC, area under the receiver operating characteristic curve; CI, confidence interval.

Internal validation using 1000 bootstrap resamples yielded optimism-corrected AUCs of 0.706, 0.698, and 0.735 for the clinicopathological, CT feature, and Integrated models. The corresponding optimism-corrected Brier scores were 0.218, 0.221, and 0.208, and the calibration slopes were 0.912, 0.870, and 0.815. The differences between the optimism-corrected AUC estimates were 0.029 for the Integrated versus clinicopathological models, 0.037 for the Integrated versus CT feature models, and −0.008 for the CT features versus clinicopathological models (Supplementary Tables S4 and S5).

For the Integrated model, the optimism-corrected calibration slope of 0.815 was used as a uniform shrinkage factor. All nine slope coefficients were multiplied by 0.815, and the intercept was re-estimated to preserve calibration-in-the-large. The resulting coefficients and re-estimated intercept are reported in Supplementary Table S11.

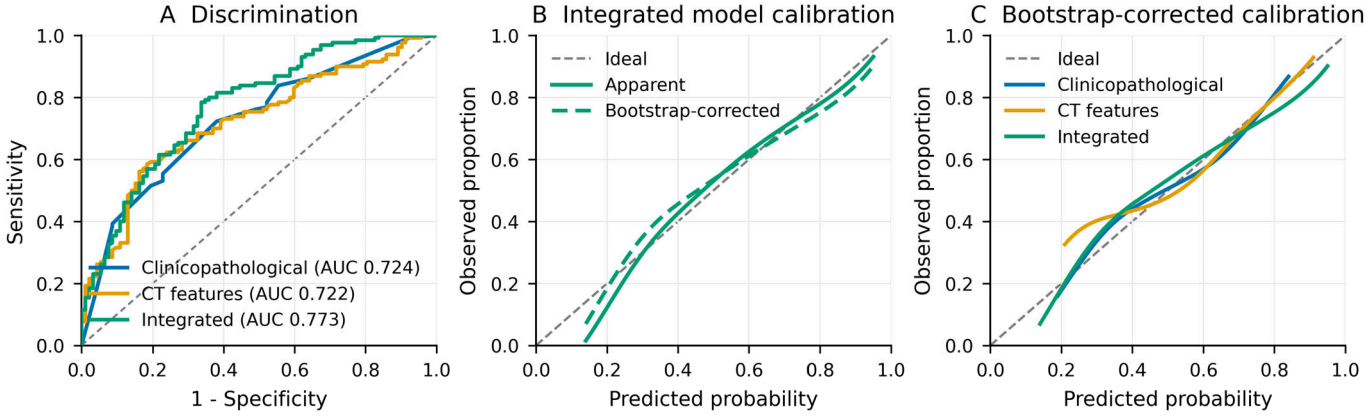


Figure 3. Discrimination and calibration of the three models in the development cohort. (**A**) Receiver operating characteristic curves for the clinicopathological, CT feature, and Integrated models under the ≥40% definition. The dashed diagonal line represents no-discrimination performance (AUC = 0.5) (**B**) Apparent calibration curves. (**C**) Optimism-corrected calibration curves derived from 1000 bootstrap resamples. The diagonal reference lines in panels (**B**,**C**) indicate ideal calibration. Optimism-corrected performance estimates are reported in Supplementary Table S4. AUC, area under the receiver operating characteristic curve.

3.6. Expression-Probability Gradient

The Integrated model was developed for the primary ≥ 40% outcome. Following uniform shrinkage of all nine slope coefficients and re-estimation of the intercept, the resulting probabilities were used in the expression-gradient analyses. The cohort comprised 92 tumours with <40% expression, 30 with 40–74% expression, and 100 with ≥75% expression. Probabilities derived from the uniformly shrunken Integrated model increased across the <40%, 40–74%, and ≥75% expression strata, with median values of 0.472 (IQR, 0.323–0.604), 0.579 (IQR, 0.414–0.726), and 0.717 (IQR, 0.551–0.830), respectively. The overall difference was significant (Kruskal–Wallis H = 56.71; $p = 4.85 \times 10^{-13}$; epsilon squared = 0.250), and the Integrated-model score was positively associated with the ordered expression strata (Kendall tau-b = 0.401; $p = 2.80 \times 10^{-14}$) (Figure 4A and Supplementary Table S6). Pairwise comparisons showed that the model-derived probabilities were higher in the ≥75% group than in the 40–74% group (Cliff's delta for 40–74% versus ≥75% = −0.386, 95% CI, −0.589 to −0.163; Holm-adjusted $p = 0.006$).

Across quintiles of the Integrated-model score, positivity increased from 22.2% to 84.4% under the ≥40% definition and from 6.7% to 75.6% under the ≥75% definition (both trends $p < 0.001$; Figure 4B and Supplementary Table S7). When the same uniformly shrunken Integrated-model score was applied to the ≥75% outcome without outcome-specific coefficient estimation, the AUC was 0.781 (bootstrap 95% CI, 0.718–0.836). Because all ≥75% cases had been labelled positive under the ≥40% development outcome, this within-cohort discrimination was partly expected by construction.

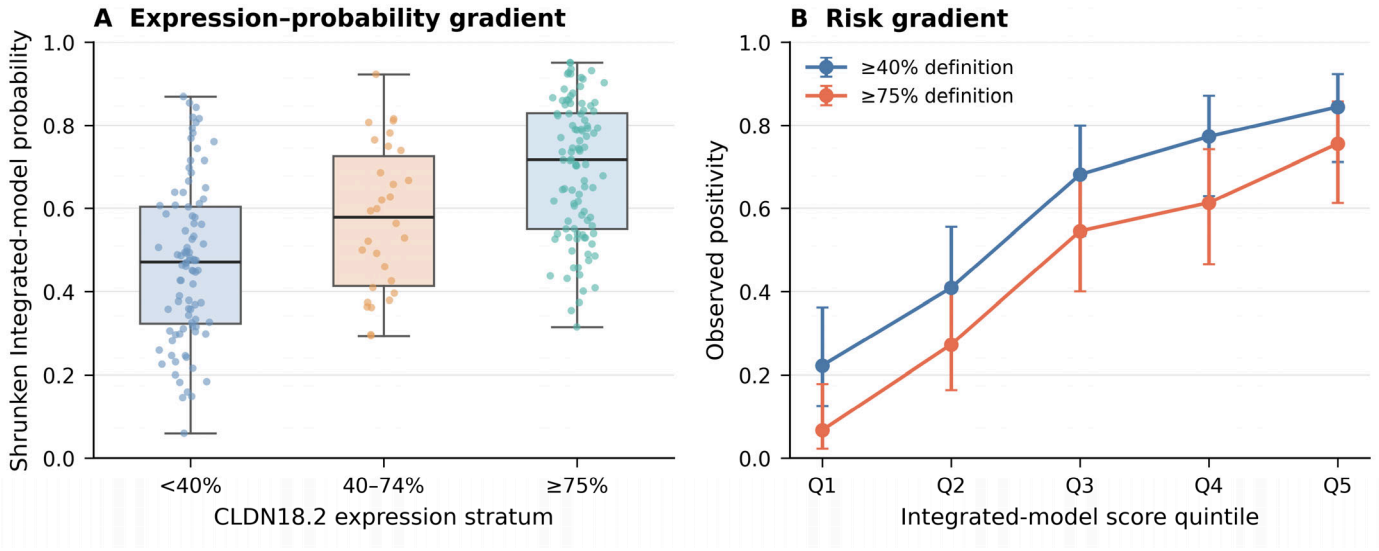


Figure 4. Expression and risk gradients based on the uniformly shrunken Integrated model. (**A**) Uniformly shrunken Integrated-model probabilities across the <40%, 40–74%, and ≥75% CLDN18.2 expression strata. Boxes indicate the interquartile range, horizontal lines indicate medians, and whiskers extend to 1.5 times the interquartile range. (**B**) Observed CLDN18.2 positivity rates across quintiles of the shrunken Integrated-model score. Error bars indicate 95% Wilson confidence intervals. All nine slope coefficients were multiplied by 0.815, and the model intercept was re-estimated to preserve calibration-in-the-large.

3.7. Exploratory Analyses

The full-cohort Integrated-model scores were applied to the HER2-defined subgroups without subgroup-specific refitting. In the HER2-negative subgroup (n = 193), the CT features and Integrated models achieved AUCs of 0.719 (95% bootstrap CI, 0.645–0.791) and 0.757 (95% bootstrap CI, 0.684–0.830), respectively. In the HER2-positive subgroup (n = 29), the corresponding AUCs were 0.737 (95% bootstrap CI, 0.511–0.927) and 0.778 (95% bootstrap CI, 0.561–0.929).

In the sensitivity analyses of CLDN18.2 expression as an ordinal or continuous outcome, the proportional-odds model yielded a mean cross-validated ordinal C-index of 0.718 and a macro-averaged one-versus-rest AUC of 0.669. Across 50 repeated stratified 10-fold cross-validation runs, the mean class-specific AUCs were 0.726, 0.535, and 0.746 for the <40%, 40–74%, and ≥75% expression groups, respectively. The fractional logistic model yielded a mean cross-validated R^2 of 0.217 and a Spearman correlation of 0.466 between the observed and predicted expression percentages. Additional results are provided in Supplementary Tables S8–S10 and Supplementary Figures S1 and S2. Representative CT and CLDN18.2 immunohistochemical findings from a patient with CLDN18.2-positive gastric cancer are shown in Figure 5.

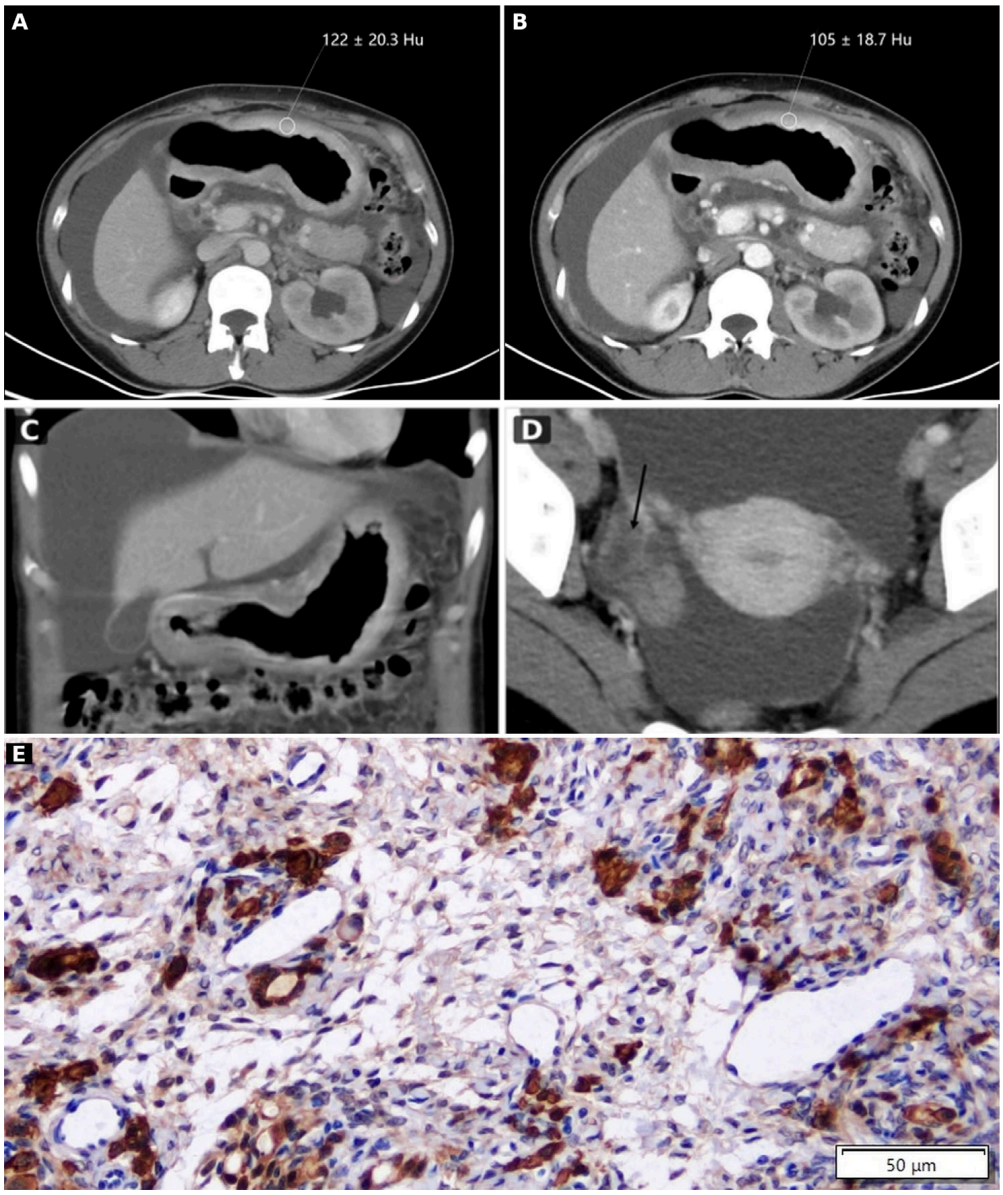


Figure 5. Representative CT and CLDN18.2 immunohistochemical findings in a patient with CLDN18.2-positive gastric cancer. (**A**) Venous-phase axial CT shows the diffuse thickening and enhancement of the gastric wall. A circular region of interest was placed at the site of greatest tumour thickness on the image showing the maximal tumour extent, yielding a mean attenuation of 122 ± 20.3 HU. (**B**) On the corresponding arterial-phase image, a matched region of interest of similar size was placed at the corresponding tumour location, yielding a mean attenuation of 105 ± 18.7 HU. The tumour reached peak enhancement during the venous phase. (**C**) Coronal CT demonstrates diffuse gastric wall thickening extending from the fundus through the body to the antrum, consistent with Borrmann type IV gastric cancer. (**D**) Pelvic CT shows a cystic and solid lesion in the right ovarian region, indicated by the arrow, consistent with ovarian metastasis. Large-volume abdominopelvic ascites is also present. (**E**) CLDN18.2 immunohistochemistry from the same patient shows a representative field of poorly differentiated adenocarcinoma. Brown chromogen highlights membranous CLDN18.2 expression in tumour cells, with tumour cell nuclei counterstained dark blue. On whole-section assessment, moderate-to-strong membranous staining was present in 90% of tumour cells. Scale bar, 50 µm.

4. Discussion

This study identified an interpretable and reproducible macroscopic phenotype on routine contrast-enhanced CT that was associated with CLDN18.2 expression in gastric cancer. In 222 untreated patients, the Integrated model showed the highest apparent discrimination (AUC = 0.773), with an optimism-corrected AUC of 0.735. An optimism-corrected calibration slope of 0.815 indicated some overfitting; therefore, we applied uniform coefficient shrinkage. Integrated-model probabilities increased across the <40%, 40–74%, and ≥75% expression strata, and the cross-validated ordinal model supported an association with ordered expression categories. But the predictor profile could not accurately estimate the staining percentage in individual tumours. When applied without refitting to the ≥75% outcome, the Integrated model yielded an AUC of 0.781. Although this result does not establish generalisability beyond the ≥40% threshold used for model development, the overall findings indicate that routine CT can provide complementary whole-lesion information associated with CLDN18.2 expression, while IHC remains essential to determining biomarker status.

Several studies have investigated imaging correlates of CLDN18.2 expression in gastric cancer. First-in-human PET studies using the CLDN18.2-targeted tracers ^{124}I-18B10(10L) and ^{68}Ga-NC-BCH showed the feasibility of whole-body target mapping, with tracer uptake patterns corresponding to CLDN18.2 expression assessed by immunohistochemistry [18,19]. Target-specific PET may therefore provide information on the distribution of CLDN18.2 across lesions, although current evidence remains limited to small early translational cohorts. Complementing these clinical studies, a preclinical study from the United States demonstrated specific tumour uptake of ^{89}Zr-labelled zolbetuximab in gastric and pancreatic cancer xenograft models, supporting further investigation of CLDN18.2-directed imaging and radiotheranostic strategies [20]. Using conventional ^{18}F-FDG PET/CT, Yin et al. found lower SUVmax and total lesion glycolysis in CLDN18.2-positive metastatic gastric cancers [21]. A subsequent study of 291 patients combined PET/CT radiomics with clinical variables and achieved an AUC of 0.765 in a held-out validation cohort, indicating that PET/CT-derived features may provide information associated with CLDN18.2 status [22]. CT radiomics studies have provided complementary evidence. A peritumoral radiomics model showed numerically higher validation performance than its intratumoural counterpart, and a clinico-radiomic nomogram incorporating CA19-9, Borrmann type, and the peritumoral radiomics score achieved an AUC of 0.820 in the validation cohort [23]. A recent habitat radiomics study based on dual-layer spectral detector CT achieved a test-set AUC of 0.757 for a model combining habitat features with clinical variables, suggesting that spatially resolved spectral information may also contribute to CLDN18.2 assessment [24]. Our study extends this evidence by deriving a low-dimensional, interpretable phenotype using features that can be directly observed or measured on routinely acquired contrast-enhanced CT, without requiring a dedicated radiotracer or high-dimensional feature extraction.

Together, the predictors included in the integrated model described a clinically interpretable macroscopic phenotype associated with CLDN18.2 expression. In the multivariable analysis, age > 60 years, HER2 positivity, and esophagogastric junction involvement were associated with lower odds of CLDN18.2 positivity, whereas signet-ring cell carcinoma, Borrmann type IV morphology, and distant metastasis were associated with higher odds. The associations with signet-ring cell carcinoma and Borrmann type IV morphology are consistent with findings from international cohorts. A global analysis of the SPOTLIGHT and GLOW populations found the highest prevalence of CLDN18.2 positivity in diffuse-type tumours, while studies from Japan and the United States reported associations with Borrmann type IV morphology and signet-ring-cell features, respectively [26–28]. In the univariable analysis, diffuse Lauren type and signet-ring cell histology were also more

frequent among CLDN18.2-positive tumours, in keeping with previous clinicopathological studies [26,28]. Arterial-phase tumour attenuation showed a positive association of borderline statistical significance ($p = 0.051$), suggesting that perfusion-related information may contribute to the imaging phenotype. The biological basis of this association was not investigated in the present study. Reported associations between CLDN18.2 expression and metastatic distribution have varied across cohorts and positivity thresholds. A Korean study found the highest CLDN18.2 positivity in peritoneal lesions and the lowest in liver lesions, whereas an international cohort observed an association with peritoneal metastasis at the ≥50% cutoff but not at the ≥75% cutoff [9,29]. Because distant metastasis was coded as a binary variable in our model, this finding does not identify a CLDN18.2-specific metastatic pattern. Sex and clustered peritumoral lymph nodes were retained in the data-informed predictor set but were not independently associated with CLDN18.2 positivity in the multivariable model. The evaluated CT features also showed good reproducibility: continuous measurements had ICCs of 0.891–1.000, and 19 of the 20 categorical features demonstrated good interobserver agreement, including substantial agreement for peak enhancement phase (k = 0.788).

Beyond binary classification, Integrated-model probabilities increased progressively across the <40%, 40–74%, and ≥75% CLDN18.2 expression strata, with a substantial between-group effect ($\varepsilon^2 = 0.250$) and a moderate ordinal association (Kendall's $\tau b = 0.401$). Although both the 40–74% and ≥75% groups were classified as positive under the ≥40% definition used for model development, probabilities were higher in the ≥75% group, with a moderate between-group effect (Cliff's delta = −0.386, 95% CI: −0.589 to −0.163; Holm-adjusted $p = 0.006$). These findings indicate a group-level association between the predictor profile and ordered expression categories but do not imply accurate estimation of the expression percentage in individual tumours. The ordinal model showed moderate overall ranking performance in repeated cross-validation, with an ordinal C-index of 0.718 and a macro-averaged one-versus-rest AUC of 0.669. However, the class-specific AUC for the 40–74% intermediate-expression group was only 0.535. This limitation is consistent with the cumulative structure of the proportional-odds model, which evaluates ordering across thresholds rather than directly separating the middle category from both adjacent groups. Thus, an overall ordinal association does not imply reliable identification of the intermediate-expression group, and this distinction warrants further investigation in larger independent cohorts. Similarly, the fractional logistic model explained only 21.7% of the variance in continuous CLDN18.2 expression, with a Spearman correlation of 0.466, indicating limited ability to estimate the staining percentage in individual tumours. When applied directly to the ≥75% outcome without refitting, the Integrated model yielded an AUC of 0.781. Because tumours meeting the ≥75% definition were included within the positive class used for model development, some discrimination was structurally expected. Nevertheless, this result provides a basis for future external studies to determine whether the CT phenotype retains informative ranking across clinically relevant expression thresholds.

Routine CT may complement tissue-based CLDN18.2 assessment but cannot replace immunohistochemical testing. Current guidance supports assessing HER2 and CLDN18.2 as part of the predictive biomarker work-up for advanced gastric or gastro-oesophageal junction adenocarcinoma, preferably alongside PD-L1 and MMR/MSI [1,30,31]. Endoscopic biopsy generally provides tissue for histological diagnosis and initial biomarker testing before or alongside staging CT [1,31]. Therefore, the CT model developed in this study should not be used to select patients for initial CLDN18.2 testing. The CT features and clinicopathological models showed comparable discrimination, whereas the Integrated model provided modest incremental discrimination over the clinicopathological model, supporting the role of CT as a complementary source of information. Once the IHC result

is available, the relative probability derived from the CT feature model can be considered alongside the tissue result to assess imaging–pathology concordance. A relatively higher CT-derived probability that is discordant with a negative or technically uncertain IHC result may serve as an incremental signal to review gastric distension and image quality, specimen adequacy and tumour-cell content, staining quality, and potential spatial heterogeneity. If the discordance remains clinically relevant after this review, it may inform multidisciplinary consideration of testing another tissue block or an available alternative specimen, or obtaining additional samples. The CT finding alone should not determine whether repeat biopsy is performed. Conversely, a relatively lower CT-derived probability should not override a positive IHC result. Figure 6 therefore presents a conceptual framework for reviewing CT–IHC concordance and discordance, without defining a clinical decision threshold. IHC remains the reference standard for determining CLDN18.2 status.

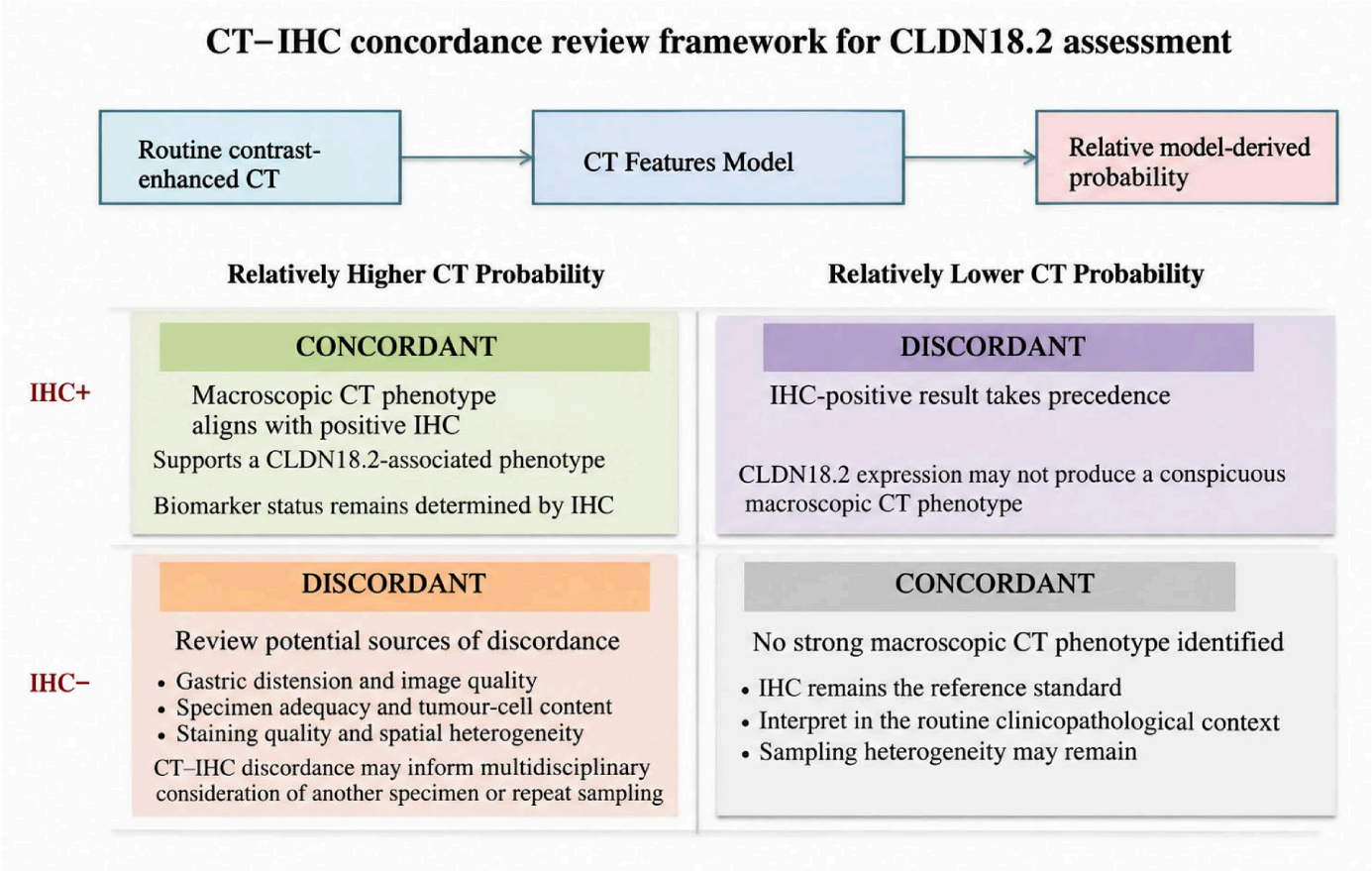


Figure 6. Conceptual CT–IHC concordance framework for CLDN18.2 assessment. Relative probabilities derived from the CT feature model are cross-classified with CLDN18.2 immunohistochemistry results. Concordant findings indicate agreement between the macroscopic CT phenotype and tissue assessment. A relatively higher CT-derived probability accompanied by negative immunohistochemistry may serve as an incremental signal to review gastric distension and image quality, specimen adequacy and tumour-cell content, staining quality, and spatial heterogeneity and may inform multidisciplinary consideration of testing another tissue block or specimen or obtaining additional samples. When immunohistochemistry is positive despite a relatively lower CT-derived probability, the immunohistochemical result takes precedence, indicating that CLDN18.2 expression may not produce a conspicuous macroscopic CT phenotype. Relatively higher and lower probabilities represent conceptual strata rather than externally validated clinical decision thresholds. The CT-derived probability should not be used to omit CLDN18.2 testing or override the immunohistochemical result. IHC remains the reference standard for CLDN18.2 classification and biomarker-based treatment selection. CT, computed tomography; IHC, immunohistochemistry.

Accurate CLDN18.2 assessment is clinically relevant because zolbetuximab is a treatment option for patients with HER2-negative, CLDN18.2-positive advanced gastric or gastro-oesophageal junction adenocarcinoma [3,4,30]. Coexpression of HER2 and CLDN18.2 was observed in this cohort, with 11 of 29 HER2-positive patients meeting the study-defined ≥40% threshold for CLDN18.2 positivity. In this small subgroup, the Integrated model achieved an apparent AUC of 0.778, although the confidence interval was wide. This exploratory analysis indicates that the imaging phenotype was not confined to HER2-negative tumours, but the subgroup was too small to establish model performance in HER2-positive disease.

This study had several limitations. The retrospective single-centre design and modest sample size may have introduced selection bias and limited the transportability of the findings, and no independent test set or external validation cohort was available. Although bootstrap validation re-estimated the model coefficients within each resample, it used the fixed data-informed predictor sets and did not repeat the preliminary candidate-screening process. The optimism-corrected estimates may not fully capture uncertainty arising from predictor selection. The expression-gradient, ≥75% cross-definition, ordinal, continuous expression, and HER2 subgroup analyses were all conducted within the development cohort and should therefore be regarded as within-cohort secondary analyses. The tissue-based reference standard may also be affected by limited tumour content, spatial heterogeneity, and variability in staining interpretation [8,11,31]. Interobserver variability in CLDN18.2 scoring was not quantified, and the antibody platform used in this study differs from the companion diagnostic assay used in the pivotal zolbetuximab trials. The potential incremental value of dual-energy or spectral CT parameters was not evaluated. Finally, the CT–IHC concordance framework in Figure 6 is conceptual and does not provide a validated probability threshold or clinical decision rule. Future multicentre studies should externally validate model discrimination and calibration across imaging protocols and patient populations, assess the need for recalibration, and prospectively evaluate whether CT–IHC discordance can improve the recognition of potentially unrepresentative tissue results and inform pathology review, the testing of alternative specimens, or repeat sampling.

5. Conclusions

In conclusion, this study identified an interpretable and reproducible macroscopic phenotype on routine contrast-enhanced CT that was associated with CLDN18.2 expression in gastric cancer. The phenotype was associated with ordered expression categories but did not reliably distinguish the 40–74% intermediate-expression group or accurately estimate the staining percentage in individual tumours. The CT model is not intended to select patients for initial CLDN18.2 testing; its potential value lies in providing complementary whole-lesion information when CT and IHC findings are discordant. In this setting, the CT-derived probability may prompt review of specimen adequacy, staining quality, and spatial heterogeneity and may inform multidisciplinary consideration of further tissue evaluation, but it should not determine repeat biopsy on its own. IHC remains the reference standard for determining CLDN18.2 status and guiding biomarker-directed treatment selection, and multicentre external validation and prospective evaluation are required before clinical implementation.

Supplementary Materials: The following supporting information can be downloaded at: https://www.mdpi.com/article/10.3390/curroncol33120743/s1, Supplementary Methods: additional details of CT acquisition and gastric preparation; Method S1: Candidate predictor selection and model specification; Method S2: Model comparisons and internal validation; Method S3: Expression-gradient, cross-definition, and subgroup analyses; Method S4: Ordinal and continuous expression sensitivity analyses; Supplementary Results: equations and variable coding for the final clinicopatho-

logical, CT feature, and Integrated models for the ≥40% definition; Table S1: Representative CT images and measurement schematics of subjective imaging signs; Table S2: Interobserver agreement and Bland–Altman results for continuous CT measurements; Table S3: Interobserver agreement for categorical CT features; Table S4: Bootstrap-corrected performance of the three models; Table S5: Incremental model comparisons; Table S6: Integrated-model probabilities across CLDN18.2 expression strata; Table S7: Observed CLDN18.2 positivity across Integrated-model-score quintiles; Table S8: Cross-definition discrimination and exploratory HER2 subgroup analyses; Table S9: Ordinal and fractional logistic expression models; Table S10: Performance from 50 repeated stratified 10-fold cross-validation runs; Table S11: Uniformly shrunken coefficients and re-estimated intercepts for the prediction models.; Figure S1: Discrimination in HER2-defined subgroups; Figure S2: Cross-validated ordinal and continuous expression predictions. File S1: TRIPOD checklist [25].

Author Contributions: Conceptualization, L.T. and Y.S.; methodology, F.H., Y.L. and J.C.; validation, X.L.; formal analysis, J.C.; investigation, F.H., Y.L., J.C., W.J. and J.L.; data curation, F.H., Y.L. and W.J.; writing—original draft preparation, F.H. and Y.L.; writing—review and editing, F.H., J.C., Y.L., W.J., J.L., X.L., Y.S., X.Z. and L.T.; supervision, L.T., Y.S. and X.Z.; project administration, L.T., Y.S. and X.L. provided expert statistical guidance during the revision, F.H. and X.L. jointly conducted and verified the revised statistical analyses. All authors have read and agreed to the published version of the manuscript. F.H. and Y.L. contributed equally to this work.

Funding: This work was supported by the Noncommunicable Chronic Diseases–National Science and Technology Major Project, grant number 2024ZD0520600, and the National Natural Science Foundation of China, grant numbers U24A20759, 82441018, and 92459302. The funding bodies had no role in the study design; data collection, analysis, or interpretation; preparation of the manuscript; or the decision to submit the manuscript for publication.

Institutional Review Board Statement: This study was conducted in accordance with the Declaration of Helsinki and was approved by the Ethics Committee of Peking University Cancer Hospital (protocol code 2023KT59; date of approval: 9 May 2023).

Informed Consent Statement: The requirement for informed consent to participate was waived by the Ethics Committee of Peking University Cancer Hospital because of the retrospective nature of the study. Figure 5 displays fully de-identified CT and histopathological images, ensuring that no patient-identifiable information is included.

Data Availability Statement: The datasets generated and/or analysed during the current study are not publicly available because they contain patient-level clinical, pathological, and imaging data that are subject to patient privacy and institutional data-protection requirements. Data may be made available from the corresponding author upon reasonable request, subject to additional approval by the institutional data management authority and compliance with applicable ethical and data-protection requirements.

Conflicts of Interest: The authors declare no conflicts of interest.

Abbreviations

Abbreviation	Definition
AUC	area under the receiver operating characteristic curve
CI	confidence interval
CA19-9	carbohydrate antigen 19-9
CLDN18.2	claudin 18 isoform 2
CT	computed tomography
EGJ	esophagogastric junction
FDG	fluorodeoxyglucose
FLOT	5-fluorouracil, leucovorin, oxaliplatin, and docetaxel
HER2	human epidermal growth factor receptor 2
HU	Hounsfield unit
ICC	intraclass correlation coefficient

IHC	immunohistochemistry
IQR	interquartile range
LN	lymph node
NTER	normalised tumour enhancement ratio
OR	odds ratio
PET	positron emission tomography
ROC	receiver operating characteristic
ROI	region of interest
SD	standard deviation
SUVmax	maximum standardised uptake value
VIF	variance inflation factor

References

1. Shitara, K.; Fleitas, T.; Kawakami, H.; Curigliano, G.; Narita, Y.; Wang, F.; Wardhani, S.O.; Basade, M.; Rha, S.Y.; Wan Zamaniah, W.I.; et al. Pan-Asian adapted ESMO Clinical Practice Guidelines for the diagnosis, treatment and follow-up of patients with gastric cancer. *ESMO Open* **2024**, *9*, 102226. [CrossRef] [PubMed]
2. Ajani, J.A.; D'Amico, T.A.; Bentrem, D.J.; Corvera, C.U.; Das, P.; Enzinger, P.C.; Enzler, T.; Gerdes, H.; Gibson, M.K.; Grierson, P.; et al. Gastric Cancer, Version 2.2025, NCCN Clinical Practice Guidelines in Oncology. *J. Natl. Compr. Cancer Netw.* **2025**, *23*, 169–191. [CrossRef] [PubMed]
3. Shitara, K.; Lordick, F.; Bang, Y.-J.; Enzinger, P.; Ilson, D.; Shah, M.A.; Van Cutsem, E.; Xu, R.-H.; Aprile, G.; Xu, J.; et al. Zolbetuximab plus mFOLFOX6 in patients with CLDN18.2-positive, HER2-negative, untreated, locally advanced unresectable or metastatic gastric or gastro-oesophageal junction adenocarcinoma (SPOTLIGHT): A multicentre, randomised, double-blind, phase 3 trial. *Lancet* **2023**, *401*, 1655–1668. [CrossRef] [PubMed]
4. Shah, M.A.; Shitara, K.; Ajani, J.A.; Bang, Y.-J.; Enzinger, P.; Ilson, D.; Lordick, F.; Van Cutsem, E.; Gallego Plazas, J.; Huang, J.; et al. Zolbetuximab plus CAPOX in CLDN18.2-positive gastric or gastroesophageal junction adenocarcinoma: The randomized, phase 3 GLOW trial. *Nat. Med.* **2023**, *29*, 2133–2141. [CrossRef] [PubMed]
5. Nakayama, I.; Qi, C.; Chen, Y.; Nakamura, Y.; Shen, L.; Shitara, K. Claudin 18.2 as a novel therapeutic target. *Nat. Rev. Clin. Oncol.* **2024**, *21*, 354–369. [CrossRef] [PubMed]
6. Sahin, U.; Koslowski, M.; Dhaene, K.; Usener, D.; Brandenburg, G.; Seitz, G.; Huber, C.; Türeci, Ö. Claudin-18 splice variant 2 is a pan-cancer target suitable for therapeutic antibody development. *Clin. Cancer Res.* **2008**, *14*, 7624–7634. [CrossRef] [PubMed]
7. Sahin, U.; Türeci, Ö.; Manikhas, G.; Lordick, F.; Rusyn, A.; Vynnychenko, I.; Dudov, A.; Bazin, I.; Bondarenko, I.; Melichar, B.; et al. FAST: A randomised phase II study of zolbetuximab plus EOX versus EOX alone for first-line treatment of advanced CLDN18.2-positive gastric and gastro-oesophageal adenocarcinoma. *Ann. Oncol.* **2021**, *32*, 609–619. [CrossRef] [PubMed]
8. Pak, S.; Simon, A.G.; Lyu, S.I.; Tolkach, Y.; Alakus, H.; Zander, T.; Buettner, R.; Bruns, C.J.; Schroeder, W.; Quaas, A. The expression of the tight junction protein and therapeutical target Claudin 18.2 is heterogeneously distributed within esophageal and gastric adenocarcinoma. *Sci. Rep.* **2025**, *15*, 28958. [CrossRef] [PubMed]
9. Choi, E.; Shin, J.; Ryu, M.-H.; Kim, H.-D.; Park, Y.S. Heterogeneity of claudin 18.2 expression in metastatic gastric cancer. *Sci. Rep.* **2024**, *14*, 17648. [CrossRef] [PubMed]
10. Yamamoto, K.; Nakayama, I.; Sakamoto, N.; Matsubara, Y.; Miyashita, Y.; Kobayashi, A.; Okazaki, U.; Okemoto, D.; Seguchi, K.; Hosokai, T.; et al. Temporal dynamics of CLDN18.2 expression following zolbetuximab treatment in advanced gastric cancer. *ESMO Gastrointest. Oncol.* **2025**, *9*, 100206. [CrossRef] [PubMed]
11. Lop Gros, J.; Santiago Díaz, P.; Larrubia Loring, M.; Patriarca, M.E.; Lloveras, B.; Iglesias, M. Claudin 18.2 immunohistochemistry expression in gastric cancer: A systematic review. *Appl. Immunohistochem. Mol. Morphol.* **2025**, *33*, 61–69. [CrossRef] [PubMed]
12. Jasani, B.; Taniere, P.; Schildhaus, H.-U.; Blighe, K.; Parry, S.; Wilkinson, D.; Atkey, N.; Clare-Antony, S.; McCabe, C.; Quinn, C.; et al. Global ring study to investigate the comparability of total assay performance of commercial Claudin 18 antibodies for evaluation in gastric cancer. *Lab. Investig.* **2024**, *104*, 100284. [CrossRef] [PubMed]
13. Li, Y.; Dai, W.-G.; Lin, Q.; Wang, Z.; Xu, H.; Chen, Y.; Wang, J. Predicting human epidermal growth factor receptor 2 status of patients with gastric cancer by computed tomography and clinical features. *Gastroenterol. Rep.* **2024**, *12*, goae042. [CrossRef] [PubMed]
14. Lee, J.S.; Kim, S.H.; Im, S.-A.; Kim, M.A.; Han, J.K. Human epidermal growth factor receptor 2 expression in unresectable gastric cancers: Relationship with CT characteristics. *Korean J. Radiol.* **2017**, *18*, 809–820. [CrossRef] [PubMed]
15. Ma, T.; Cui, J.; Wang, L.; Li, H.; Ye, Z.; Gao, X. A CT-based radiomics signature for prediction of HER2 overexpression and treatment efficacy of trastuzumab in advanced gastric cancer. *Transl. Cancer Res.* **2022**, *11*, 4326–4337. [CrossRef] [PubMed]
16. Guan, X.; Lu, N.; Zhang, J. Accurate preoperative staging and HER2 status prediction of gastric cancer by the deep learning system based on enhanced computed tomography. *Front. Oncol.* **2022**, *12*, 950185. [CrossRef] [PubMed]

17. Liu, S.; Qiao, X.; Ji, C.; Shi, H.; Wang, Y.; Li, L.; Zhou, Z. Gastric poorly cohesive carcinoma: Differentiation from tubular adenocarcinoma using nomograms based on CT findings in the 40 s late arterial phase. *Eur. Radiol.* **2021**, *31*, 5768–5778. [CrossRef] [PubMed]
18. Wang, S.; Qi, C.; Ding, J.; Li, D.; Zhang, M.; Ji, C.; Jiang, F.; Teng, F.; Yu, J.; Qian, X.; et al. First-in-human CLDN18.2 functional diagnostic PET imaging of digestive system neoplasms enables whole-body target mapping and lesion detection. *Eur. J. Nucl. Med. Mol. Imaging* **2023**, *50*, 2802–2817. [CrossRef] [PubMed]
19. Qi, C.; Guo, R.; Chen, Y.; Li, C.; Liu, C.; Zhang, M.; Zhang, C.; Zhang, X.; Hou, X.; Chen, B.; et al. 68Ga-NC-BCH whole-body PET imaging rapidly targets Claudin18.2 in lesions in gastrointestinal cancer patients. *J. Nucl. Med.* **2024**, *65*, 856–863. [CrossRef] [PubMed]
20. Raheem, S.J.; Bashyal, S.; Haj-Mirzaian, A.; Khazaei Monfared, Y.; Mahmood, U.; Heidari, P.; Strickland, M.R.; Ting, D.T.; Klempner, S.J.; Larimer, B.M.; et al. Claudin 18.2 as a Biomarker for Imaging and Radiopharmaceutical Therapy in Gastric and Pancreatic Tumors. *J. Nucl. Med.* **2026**, *67*, 113–118. [CrossRef] [PubMed]
21. Yin, H.; Luo, R.; Lv, J.; Mao, W.; Shi, H. Relationship between [18F]FDG PET/CT findings and claudin 18.2 expression in metastatic gastric cancer. *Eur. Radiol.* **2025**, *35*, 3442–3449. [CrossRef] [PubMed]
22. Sun, C.; Zhang, J.; Song, J.; Ye, X.; Xie, D.; Li, J.; Yi, H. Imaging-based stratification of Claudin 18.2-positive gastric adenocarcinoma using 18F-FDG PET/CT radiomics. *Eur. J. Nucl. Med. Mol. Imaging* **2026**, *53*, 5301–5314. [CrossRef] [PubMed]
23. Qi, W.; Jiao, M.; Wei, C.; Wang, K.; Lv, F.; Wang, X. Peritumoral CT radiomics reveals CLDN18.2-related imaging phenotypes beyond the tumor boundary in gastric cancer. *Eur. J. Radiol.* **2026**, *205*, 113246. [CrossRef] [PubMed]
24. Chen, J.; Pan, X.; Ma, H.; Tang, C.; Lu, L.; Yan, X.; Huang, J.; Tang, X.; Qian, T.; Liu, K. Prediction of Claudin18.2 expression in gastric adenocarcinoma by habitat radiomics based on spectral CT. *Sci. Rep.* **2026**, *16*, 33865. [CrossRef]
25. Collins, G.S.; Reitsma, J.B.; Altman, D.G.; Moons, K.G.M.; TRIPOD Group. Transparent reporting of a multivariable prediction model for individual prognosis or diagnosis (TRIPOD): The TRIPOD statement. *Circulation* **2015**, *131*, 211–219. [CrossRef] [PubMed]
26. Shitara, K.; Xu, R.-H.; Ajani, J.A.; Moran, D.; Guerrero, A.; Li, R.; Pavese, J.; Matsangou, M.; Bhattacharya, P.; Ueno, Y.; et al. Global prevalence of claudin 18 isoform 2 in tumors of patients with locally advanced unresectable or metastatic gastric or gastroesophageal junction adenocarcinoma. *Gastric Cancer* **2024**, *27*, 1058–1068. [CrossRef] [PubMed]
27. Kubota, Y.; Kawazoe, A.; Mishima, S.; Nakamura, Y.; Kotani, D.; Kuboki, Y.; Bando, H.; Kojima, T.; Doi, T.; Yoshino, T.; et al. Comprehensive clinical and molecular characterization of claudin 18.2 expression in advanced gastric or gastroesophageal junction cancer. *ESMO Open* **2023**, *8*, 100762. [CrossRef] [PubMed]
28. Liu, B.L.; Cleary, J.M.; Shi, J.; Hornick, J.L.; Zhao, L. Claudin 18.2 and other therapeutic biomarkers in gastric and gastroesophageal junction adenocarcinomas. *Am. J. Surg. Pathol.* **2025**, *49*, 1233–1244. [CrossRef] [PubMed]
29. Waters, R.; Sewastjanow-Silva, M.; Yamashita, K.; Abdelhakeem, A.; Iwata, K.K.; Moran, D.; Elsouda, D.; Guerrero, A.; Pizzi, M.; Rosa Vicentini, E.; et al. Retrospective study of Claudin 18 isoform 2 prevalence and prognostic association in gastric and gastroesophageal junction adenocarcinoma. *JCO Precis. Oncol.* **2024**, *8*, e2300543. [CrossRef] [PubMed]
30. Shah, M.A.; Marzalik, J.S.; Kennedy, E.B.; Deighton, D.; Hamedi, Z.; Jhawer, M.; Kadakia, K.C.; Montenegro, P.; Mukherjee, S.; Nevala-Plagemann, C.; et al. Immunotherapy and targeted therapy for advanced gastroesophageal cancer: ASCO Living Guideline, Version 2026.1.2. *J. Clin. Oncol.* **2026**, *44*, e170–e183. [CrossRef] [PubMed]
31. Brezden-Masley, C.; Fiset, P.O.; Cheung, C.C.; Arnason, T.; Bateman, J.; Borduas, M.; Evaristo, G.; Ionescu, D.N.; Lim, H.J.; Sheffield, B.S.; et al. Canadian consensus recommendations for predictive biomarker testing in gastric and gastroesophageal junction adenocarcinoma. *Curr. Oncol.* **2024**, *31*, 7770–7786. [CrossRef] [PubMed]

Disclaimer/Publisher's Note: The statements, opinions and data contained in all publications are solely those of the individual author(s) and contributor(s) and not of MDPI and/or the editor(s). MDPI and/or the editor(s) disclaim responsibility for any injury to people or property resulting from any ideas, methods, instructions or products referred to in the content.